

# Wideband Quantum Transduction for Rydberg Atomic Receivers Using Six-Wave Mixing

Yuanbin Chen, Chau Yuen, *Fellow, IEEE* Chong Meng Samson See, *Member, IEEE*

arXiv:2602.13955v1 [quant-ph] 15 Feb 2026

**Abstract**—Rydberg atomic receivers hold extremely high sensitivity to electric fields, yet their effective 3-dB baseband bandwidth under conventional electromagnetically induced transparency (EIT) is typically constrained to tens to a few hundreds of kilohertz, which hinders wideband wireless applications. To relax this bottleneck, we investigate a six-wave mixing (SWM)-based Rydberg atomic receiver as a wideband radio frequency (RF)-to-optical quantum transducer. Specifically, we develop an explicit baseband input-output model spanning from the probe input to the output light field. Based upon this model, a closed-form 3-dB bandwidth expression is derived to expose its dependence on key optical and RF parameters. We further quantify the linear dynamic range by employing the 1-dB compression point (P1dB) and the input-referred third-order intercept point (IIP3), unveiling a communication-compatible characterization of the bandwidth-linearity trade-off. Finally, our numerical results demonstrate that, given identical optical driving conditions, the SWM configuration increases the 3-dB baseband bandwidth by more than an order of magnitude compared to the EIT-based counterpart, while retaining comparable electric-field sensitivity and revealing a broad, tunable linear operating region.

**Index Terms**—Quantum sensing, Rydberg atomic receivers, six-wave mixing, quantum transduction.

## I. INTRODUCTION

Quantum information technologies have matured from largely theoretical constructs into viable platforms for computing and secure communications, and another pillar has now come to the fore: quantum sensing [1]–[4]. By coherently mapping external stimuli, such as magnetic and electric fields, inertial forces, or tiny variations in gravity, onto well-controlled quantum degrees of freedom, quantum sensors can detect weak signals with sensitivities beyond the reach of classical systems. Among the most profound shifts driven by quantum innovation in wireless communications and sensing is the emergence of Rydberg atomic receivers. These devices leverage the extreme sensitivity of highly excited Rydberg atoms, which function as radio frequency (RF)-to-optical quantum “antennas” that transduce incident RF signals into optical signatures with unprecedented precision [5]–[9].

Rydberg atomic receivers depart fundamentally from conventional dipole-antenna-based RF front-ends. Instead of converting RF signals into currents in metal structures followed by low-noise amplifiers (LNA), a vapor of alkali atoms (typically rubidium or cesium) is optically driven into Rydberg states having enormous electric dipole moments and polarizabilities, so that even a minute RF field

Yuanbin Chen and Chau Yuen are with the School of Electrical and Electronics Engineering, Nanyang Technological University, Singapore 639798 (emails: yuanbin.chen@ntu.edu.sg; chau.yuen@ntu.edu.sg).

Chong Meng Samson See is with DSO National Laboratories, Singapore 118225 (e-mail: schongme@dsorg.org.sg).

produces a resolvable Stark shift or Autler-Townes (AT) splitting in an electromagnetically induced transparency (EIT) resonance [4], [10]. In other words, the atomic ensemble facilitates a coherent RF-to-optical conversion process: an incoming RF field disturbs the Rydberg manifold, and this disturbance is encoded onto the probe transmission spectrum as a readily detectable optical signal. The optical readout of the EIT spectra allows simultaneous extraction of key parameters: the amplitude of the incident field [11]–[14], its polarization state [15]–[18], and both the magnitude and orientation of an applied magnetic field [19], [20]. By leveraging EIT technique, the Rydberg atomic receivers having a single vapor cell have demonstrated the projected electric-field noise floor on the order of  $\sim 0.01 \text{ nV/cm}/\sqrt{\text{Hz}}$  in the standard quantum limit (SQL) regime [21], which is orders of magnitude far below the thermal noise floor of approximately  $\sim 0.98 \text{ nV/cm}/\sqrt{\text{Hz}}$  [22] used to benchmark classical receivers. Additionally, the dense manifold of Rydberg transitions supports carrier frequencies from near-DC up to the Terahertz (THz) regime within a single physical platform [4].

Despite these benefits, a significant constraint of current Rydberg atomic receivers is their intrinsically limited instantaneous bandwidth. In the canonical EIT-based scheme, the RF field slightly shifts the EIT resonance, so that its modulation is converted into small changes in the probe transmission and phase around the steep dispersion slope of a narrow transparency window [23]–[25]. The effective 3-dB RF bandwidth is therefore tied to the full-width at half-maximum (FWHM) of this EIT resonance, determined by the decoherence rates of the ground-state and Rydberg coherences, in addition to laser linewidth and transit-time broadening. To maintain quantum-limited sensitivity, one typically employs low probe power and moderate coupling strengths, which suppresses power broadening but additionally narrows the EIT window. Consequently, EIT-based Rydberg receivers often demonstrate practical baseband bandwidths limited to tens or a few hundreds of kilohertz, resulting in a fundamental tension between high sensitivity and the extensive signal bandwidths required for wideband wireless communications.

A viable approach to relax this bandwidth bottleneck is to move beyond simple three- or four-level EIT and exploit higher-order nonlinear processes such as six-wave mixing (SWM) in multi-level Rydberg manifolds [26]–[30]. In SWM-based schemes, a set of auxiliary optical fields, together with the RF field to be detected, drive a closed loop of atomic transitions, generating a new optical field whose amplitude and phase carry the full RF information. By appropriately dressing the Rydberg states and shifting

oscillator strength among multiple optical channels, the SWM process can substantially broaden the spectral response of the generated light field, yielding a much larger FWHM of the SWM signal than that of the underlying EIT resonance. This intuition is supported by recent experiments presented in [29], in which the proposed Rydberg photonic converter exhibits an RF-to-optical conversion bandwidth of 16 MHz while achieving an electric-field sensitivity of approximately  $\sim 3.98 \text{ nV/cm}/\sqrt{\text{Hz}}$ . From a communication perspective, however, it is crucial to recognize that this “bandwidth enhancement” characterizes solely the expanded FWHM of the SWM optical spectrum. The end-to-end 3-dB signal bandwidth of the RF-to-optical transduction chain, which ultimately determines the effective baseband bandwidth and the performance of Rydberg atomic receivers in wideband wireless applications, have not been explicitly addressed.

From a communication-system perspective, two critical gaps remain before SWM-based Rydberg atomic receivers can be treated as bona fide wideband front-ends. Firstly, existing efforts, despite being based on atomic-physics tests, falls short to establish an explicit, closed-form input–output model that links the probe (and auxiliary) laser fields to the final electrical readout [28], [29]. Secondly, while experiments demonstrated that SWM-based Rydberg receivers can achieve sensitivities on the order of  $\sim \text{nV/cm}/\sqrt{\text{Hz}}$  and achieve signal-to-noise ratio (SNR) gains of tens of decibels under SQL conditions, these results are typically obtained within baseband bandwidths of only a few hundred kilohertz [21]–[25]. Consequently, the use of SWM to systematically engineer and quantify the effective 3-dB communication bandwidth, while preserving quantum-limited sensitivity, remains unexplored, particularly for wideband wireless designs.

Geared towards open issues mentioned above, this work fills the gap in the advancement of wideband quantum transduction for Rydberg atomic receivers. The main contributions are summarized as follows.

- We formulate a six-level SWM-based Rydberg atomic receiver as a wideband RF-to-optical quantum transducer, in which the probe, coupling, local oscillator (LO), and auxiliary optical fields, together with the RF signal, drive a closed six-wave-mixing loop that generates an output optical field whose complex envelope carry the full RF information. Beginning with the Hamiltonian and master equation, we eliminate intermediate coherences to derive a closed-form expression for the SWM coherence and fifth-order polarization. Next, we develop an explicit wideband baseband model spanning from the probe input to the output light field. This yields, to the best of our knowledge, the first compact input–output baseband model for SWM-based Rydberg atomic receivers, bridging high-order nonlinear atomic dynamics with a communication-oriented system for wideband quantum transduction analysis.
- Relying upon this model, we demonstrate that the six-level SWM chain reduces to an effective two-pole low-pass element and formulate closed-form expressions for its 3-dB bandwidth, explicitly in terms of the dressed dephasing rates of the two highest Rydberg levels and

the auxiliary-field Rabi frequency. To quantify the linear dynamic range of the SWM-based Rydberg atomic receiver considered, we analyze the 1-dB compression point (P1dB) and the input-referred third-order intercept point (IIP3), standard RF figures of merit that mark the onset of gain compression and third-order intermodulation distortion in the RF-to-optical transduction chain.

- We numerically evaluate the proposed SWM-based Rydberg atomic receiver using the QuTiP toolbox [31]. Relative to a conventional four-level EIT architecture, our simulations reveal three key features. Firstly, given identical optical driving conditions, the SWM scheme increases the 3-dB baseband bandwidth from  $\sim 0.66 \text{ MHz}$  (EIT) to  $\sim 7.2 \text{ MHz}$  while retaining comparable sensitivity. Secondly, the auxiliary field employed in the SWM configuration acts as a robust “bandwidth knob”: increasing the Rabi frequency of the auxiliary field not only broadens the effective 3-dB bandwidth, but also improves the IIP3 over a wide operating range, indicative of a better linearity. Finally, by mapping out the joint bandwidth–linearity design space, we find that the SWM-based receiver offers a smooth and benign trade-off between 3-dB bandwidth and IIP3, whereas the EIT configuration exhibits a narrow high-linearity sweet spot that is intrinsically more suitable for narrowband operation.

The remainder of this paper is structured as follows. Sec. II introduces the fundamentals of the six-level SWM-based Rydberg atomic receiver and derives the RF-to-optical baseband transfer response. Sec. III analyzes the small-signal response and linearity, yielding closed-form expressions for the 3-dB bandwidth, P1dB, and IIP3 of the proposed architecture. Sec. IV presents numerical results to validate our analytical model, to compare the SWM and EIT schemes, and to elucidate the bandwidth-linearity trade-offs. Finally, Sec. V concludes the paper.

## II. SYSTEM MODEL

### A. Six-Level Atomic Systems and SWM Architecture

The energy levels for the SWM are shown in Fig. 1(a), and the SWM-based Rydberg atomic receiver is sketched in Fig. 1(b). In our configuration, the conversion of the input RF signal into the output light field (L) is achieved via frequency mixing with four driving fields: the probe field (P), the coupling field (C), the strong LO, and the auxiliary optical field (A), in a cloud of cold  $^{87}\text{Rb}$  atoms. In this regime, the atomic thermal velocity is sufficiently small so that Doppler broadening and velocity averaging can be neglected, and collision/pressure broadening is also strongly suppressed compared with hot-vapor cells. Starting from the ground state  $|1\rangle$ , these optical fields together with the RF signal, all tuned close to their respective atomic transitions, build up a coherence between the initial state  $|1\rangle$  and the highest Rydberg state  $|6\rangle$ . On top of this configuration, a minute RF signal knocks the Rydberg coherence, so that RF signal’s amplitude and phase are imprinted onto the atomic superposition and, thus, onto the output light field (L). In this way, the SWM process serves as a coherent transducer that

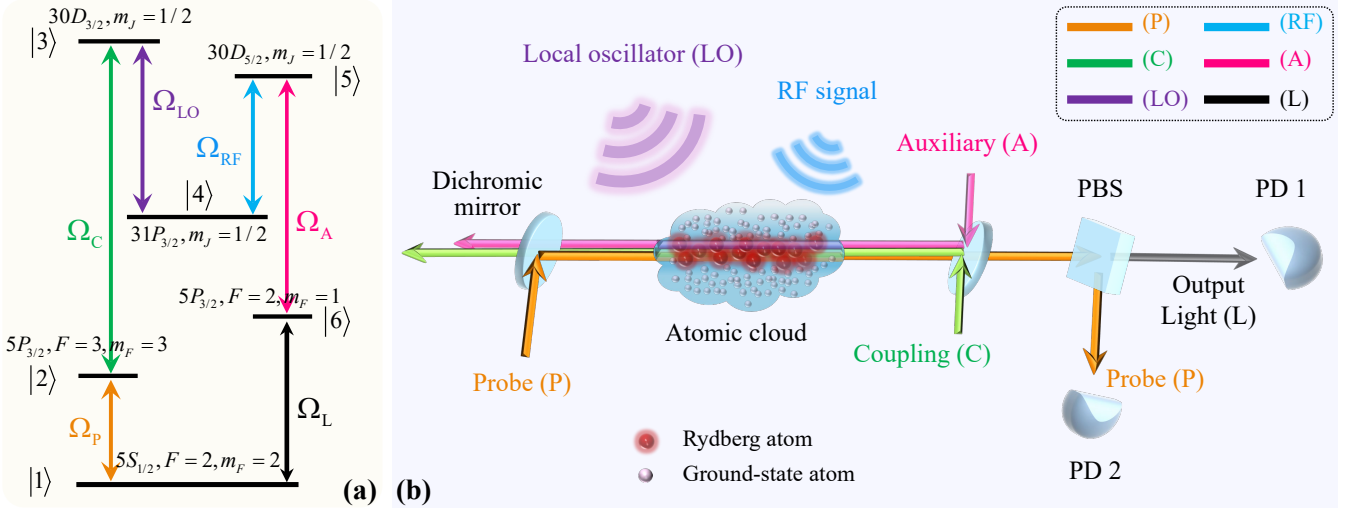


Fig. 1. Illustration of the SWM-based Rydberg atomic receiver. (a) Six-level energy transition diagram. (b) The RF signal is converted to the (output) light field by SWM-based Rydberg atomic receiver.

maps small RF-induced changes of the Rydberg coherence into measurable optical signatures. Furthermore, the P and L fields that emerge from the atomic cloud are collected by a separated employing a polarization beam splitter (PBS), as portrayed in Fig. 1(b). Their respective powers can be measured with two different avalanche photodiode detectors (PDs), i.e., PD 1 and PD 2 illustrated in Fig. 1(b). The output light field (L) has a frequency of

$$\omega_L = \omega_P + \omega_C - \omega_A + \omega_{LO} - \omega_{RF}, \quad (1)$$

which ensures that the resonant six-wave-mixing loop  $|1\rangle \xrightarrow{\Omega_P} |2\rangle \xrightarrow{\Omega_C} |3\rangle \xrightarrow{\Omega_{LO}} |4\rangle \xrightarrow{\Omega_{RF}(t)} |5\rangle \xrightarrow{\Omega_A^*} |6\rangle \xrightarrow{\Omega_L} |1\rangle$  is closed. Here,  $\omega_X$  and  $\Omega_X$  denotes the angular frequency and Rabi frequency of field  $X \in \{P, C, A, LO, RF, L\}$ , respectively.

The output optical field (L) is determined by the corresponding phase-matching condition given by

$$\mathbf{k}_L = \mathbf{k}_P + \mathbf{k}_C - \mathbf{k}_A + \mathbf{k}_{LO} - \mathbf{k}_{RF}, \quad (2)$$

where  $\mathbf{k}_X$  is the wave vector of field X.

### B. Hamiltonian and Master Equation

Under the rotating-wave approximation, the coherent evolution is characterized by a time-dependent Hamiltonian  $\hat{H}$  acting on the basis  $\{|1\rangle, \dots, |6\rangle\}$ . The Hamiltonian can be written in a compact form as

$$\hat{H} = -\frac{\hbar}{2} \begin{pmatrix} 0 & \Omega_P & 0 & 0 & 0 & 0 \\ \Omega_P^* & 2\Delta_2 & \Omega_C & 0 & 0 & 0 \\ 0 & \Omega_C^* & 2\Delta_3 & \Omega_{LO} & 0 & 0 \\ 0 & 0 & \Omega_{LO}^* & 2\Delta_4 & \Omega_{LO}(t) & 0 \\ 0 & 0 & 0 & \Omega_{RF}^*(t) & 2\Delta_5 & \Omega_A \\ 0 & 0 & 0 & 0 & \Omega_A^* & 2\Delta_6 \end{pmatrix}, \quad (3)$$

where  $\Delta_X$  represents the single-photon detuning of field  $X \in \{P, C, A, LO, RF, L\}$ , while detunings associated with levels  $|2\rangle, \dots, |6\rangle$  are defined as  $\Delta_2 = \Delta_P$ ,  $\Delta_3 = \Delta_P + \Delta_C$ ,  $\Delta_5 = \Delta_P + \Delta_C - \Delta_{LO} + \Delta_{RF}$ , and  $\Delta_6 = \Delta_L \approx 0$ .

The atomic coherences are given by the steady-state solution  $\rho$  of the following Lindblad master equation (also known as the optical Bloch equation) [12]

$$\partial_t \rho = -\frac{\jmath}{\hbar} [\hat{H}, \rho] + \mathcal{L}_\Gamma(\rho) + \mathcal{L}_{\text{depth}}(\rho). \quad (4)$$

The Lindblad term  $\mathcal{L}_\Gamma(\rho)$  (also known as population-decay Lindblad dissipator) accounts for spontaneous emission from the intermediate states  $|2\rangle$  and  $|6\rangle$  and from the Rydberg states, which is given by

$$\mathcal{L}_\Gamma(\rho) = \sum_{j>i} \Gamma_{j \rightarrow i} \mathcal{D}[|i\rangle\langle j|] \rho, \quad (5)$$

$$\mathcal{D}[|i\rangle\langle j|] \rho = [|i\rangle\langle j|] \rho [|i\rangle\langle j|]^\dagger - \frac{1}{2} \left\{ [|i\rangle\langle j|]^\dagger [|i\rangle\langle j|], \rho \right\}. \quad (6)$$

The term  $\mathcal{L}_{\text{depth}}(\rho)$  (also known as pure-dephasing Lindblad dissipator) accounts for additional dephasing mechanisms and can be written as

$$\mathcal{L}_{\text{depth}}(\rho) = \sum_{j>i} \frac{1}{2} \left[ \gamma_{ij} - \frac{1}{2} (\Gamma_i + \Gamma_j) \right] \mathcal{D}[|i\rangle\langle i| - |j\rangle\langle j|] \rho, \quad (7)$$

where  $\gamma_{ij}$  is the coherence dephasing rate and  $\Gamma_i$  represents the population decay rate associated with state  $|j\rangle$ . These rates include the effects of atomic collisions, dipole-dipole interactions between Rydberg atoms, and finite laser linewidths. The dephasing rates  $\gamma_1$ ,  $\gamma_2$ , and  $\gamma_6$  are neglected since they are much smaller than  $\Gamma$  [27], [28].

To obtain the frequency response of the SWM, we solve the linearized master equation for the first-order density matrix component  $\rho_{j1}$ . The steady-state solution  $\rho_{61}$  can be explicitly given by

$$\rho_{61}(\omega) = \left(\frac{\jmath}{2}\right)^5 \frac{\Omega_P \Omega_C \Omega_{LO}}{D_2 D_3 D_4} \frac{\Omega_A^* \Omega_{RF}(\omega)}{D_5(\omega) D_6(\omega) + \frac{|\Omega_A|^2}{4}}, \quad (8)$$

in which  $D_j(\omega) = \gamma_{j1} + \jmath(\Delta_{j1} + \omega)$ ,  $j = 2, \dots, 6$ , represents the complex detuning,  $\gamma_{j1}$  is the decoherence rate (including population decay and pure dephasing) of  $\rho_{j1}$ , and  $\Delta_j$  represents the detuning of level  $|j\rangle$  from the multi-photon

resonance. Note that since the relevant analysis frequencies  $\omega$  are much smaller than the optical detunings and dephasing rates of levels  $|2\rangle$ ,  $|3\rangle$ , and  $|4\rangle$ , we may, to an excellent approximation, neglect the  $\omega$ -dependence in  $D_2$ ,  $D_3$ , and  $D_4$ . We keep the explicit  $\omega$ -dependence only in  $D_5(\omega)$  and  $D_6(\omega)$ , which are responsible for the bandwidth of interest.

Regarding  $\rho_{61}(\omega)$ , in a density-matrix language, this parameter describes how strongly the atoms oscillate between levels  $|6\rangle$  and  $|1\rangle$  at the analysis frequency  $\omega$ . Physically, this oscillation creates an electric dipole on the  $|6\rangle \rightarrow |1\rangle$  transition. A larger  $\rho_{61}(\omega)$  leads to a stronger dipole oscillation, which in turn enhances the radiated light on this transition. When we consider an ensemble atomic cloud, these dipoles add up to a macroscopic polarization at the generated-light frequency  $\omega_L$ . This polarization is the actual source term that appears in Maxwell's equations and drives the output light field (L) [26]. Therefore, once  $\rho_{61}(\omega)$  is known, the next step is to convert it into the corresponding polarization and then into the light field (L) at the output of the atomic cloud. This provides a direct link between the RF-induced atomic dynamics and the measurable optical signal, and ultimately defines the RF-to-baseband transfer function.

### C. Optical Readout and Baseband Model

To quantitatively characterize the light field (L) at the output of the cold atomic cloud, we denote the atomic response by a fifth-order nonlinear polarization  $P^{(5)}(\omega)$ , because the output field (L) arises from mixing the minute RF field with four auxiliary fields (P, C, LO, and A). The fifth-order nonlinear polarization  $P^{(5)}(\omega, z)$  is proportional to the coherence  $\rho_{61}(\omega)$ , which has the form of

$$P^{(5)}(\omega, z) = N(z) \mu_{61} \rho_{61}(\omega), \quad (9)$$

where  $N(z)$  denotes the atomic number density along the propagation axis  $z$ , and  $\mu_{61}$  is the dipole momentum associated with transition  $|6\rangle \rightarrow |1\rangle$ . Physically,  $P^{(5)}(\omega, z)$  represents the effective “RF-driven dipole strength” of the whole atomic dynamics at position  $z$ , that is to say, it directly determines how efficiently the incident RF signal is up-converted into the output light field (L). By substituting  $\rho_{61}(\omega)$  in (8), we obtain

$$\begin{aligned} P^{(5)}(\omega, z) \\ = N(z) \mu_{61} \left(\frac{j}{2}\right)^5 \frac{\Omega_P \Omega_C \Omega_{\text{LO}}}{D_2 D_3 D_4} \frac{\Omega_A^* \Omega_{\text{RF}}(\omega)}{D_5(\omega) D_6(\omega) + \frac{|\Omega_A|^2}{4}}, \end{aligned} \quad (10)$$

where we have made explicit the dependence on the local density  $N(z)$ . Equivalently, by leveraging the usual relation between Rabi frequencies and electric fields, i.e.,  $\Omega_X = \mu_X E_X / \hbar$  ( $E_X$  for the electric-field amplitude and  $\hbar$  for reduced Planck constant) for each driven transition,  $P^{(5)}(\omega, z)$  can be restructured as

$$\begin{aligned} P^{(5)}(\omega, z) \\ = \epsilon_0 \chi_{\text{eff}}^{(5)}(\omega, z) E_P(z) E_C(z) E_{\text{LO}}(z) E_A^*(z) E_{\text{RF}}(\omega), \end{aligned} \quad (11)$$

where  $\epsilon_0$  is the permittivity in vacuum and the effective polarization absorption coefficient  $\chi_{\text{eff}}^{(5)}(\omega, z)$  is given by

$$\begin{aligned} \chi_{\text{eff}}^{(5)}(\omega, z) \\ = \left(\frac{j}{2}\right)^5 \frac{N(z)}{\epsilon_0 \hbar^5} \frac{\mu_{12} \mu_{23} \mu_{34} \mu_{45} \mu_{56} \mu_{61}}{D_2 D_3 D_4 \left[D_5(\omega) D_6(\omega) + \frac{|\Omega_A|^2}{4}\right]}. \end{aligned} \quad (12)$$

For a cold atomic cloud with a spatially varying density,  $\chi_{\text{eff}}^{(5)}(\omega, z)$  inherits the density profile  $N(z)$ , and also includes the longitudinal variation of the optical field amplitudes due to finite beam waists.

Given  $P^{(5)}(\omega, z)$ , the next step is to determine how this polarization generates an output light field (L) that we can actually detect. In a bulk medium, Maxwell's equations state that spatial changes of the electric field are driven by the material polarization. Since the weak output light field (L) co-propagates with the strong optical beams along the center of the cold atomic cloud, the coupling reduces to a one-dimensional propagation problem along the  $z$ -axis. Then, the field evolution satisfies

$$\begin{aligned} E_L(\omega) = j \frac{\omega_L}{2n_L c} E_{\text{RF}}(\omega) \\ \times \int \chi_{\text{eff}}^{(5)}(\omega, z) E_P(z) E_C(z) E_{\text{LO}}(z) E_A^*(z) dz, \end{aligned} \quad (13)$$

where  $n_L$  is the refractive index of the light field (L) at frequency  $\omega_L$  and  $c$  is the speed of light. For convenience, we now define an effective interaction length  $L_{\text{eff}}$  to absorb the longitudinal density variation and the spatial overlap of the driving fields. Let  $N_0 = N(0)$  denote the peak density at the cloud center, and then we define

$$L_{\text{eff}} \triangleq \frac{\int \frac{N(z)}{N_0} E_P(z) E_C(z) E_{\text{LO}}(z) E_A^*(z) dz}{E_P(0) E_C(0) E_{\text{LO}}(0) E_A^*(0)}, \quad (14)$$

where  $z = 0$  denotes the cloud center; hereafter, we drop this notation for ease of exposition. Then, using (12) and the fact that  $\chi_{\text{eff}}^{(5)}(\omega, z) \propto N(z)$ , the integral in (13) can be written as a compact form

$$E_L(\omega) = G_{\text{opt}}(\omega) E_{\text{RF}}(\omega), \quad (15)$$

with the optical RF-to-optical transfer function given by

$$G_{\text{opt}}(\omega) = j \frac{\omega_L L_{\text{eff}}}{2n_L c} \chi_{\text{eff}}^{(5)}(\omega) E_P E_C E_{\text{LO}} E_A^*. \quad (16)$$

By employing the effective polarization absorption coefficient  $\chi_{\text{eff}}^{(5)}$  shown in (12), one sees explicitly that  $G_{\text{opt}}(\omega)$  inherits the same two-pole low-pass structure determined by  $D_5(\omega)$  and  $D_6(\omega)$ . In the time domain, the output light field can be expressed as a convolution, i.e.,  $E_L(t) = g_{\text{opt}}(t) * E_{\text{RF}}(t)$ , where the impulse response corresponding to the two complex poles at  $-(\gamma_{51} + j\Delta_{51})$  and  $-(\gamma_{61} + j\Delta_{61})$  takes the form of

$$g_{\text{opt}}(t) = j \frac{\omega_L d}{2n_L c} \chi_0 E_P E_C E_{\text{LO}} E_A^* \quad (17)$$

$$\times \frac{e^{-(\gamma_{51} + j\Delta_{51})t} - e^{-(\gamma_{61} + j\Delta_{61})t}}{(\gamma_{61} - \gamma_{51}) + j(\Delta_{61} - \Delta_{51})} u(t), \quad (18)$$

where  $u(t)$  denotes the unit-step function.

Actually, the output light field  $E_L(t)$  is not measured directly. Instead, we interfere it with the probe beam on the same PD, and use this optical beat to convert the RF information into an electrical current. We first combine the probe field (P) and the output light field (L) on a single PD. The total optical field incident on the diode can be written as

$$E(t) = E_P e^{j\omega_P t} + E_L e^{j\omega_L t}, |E_L| \ll |E_P|, \quad (19)$$

which leads to the instantaneous optical power given by

$$\begin{aligned} P_{\text{opt}}(t) &= \frac{1}{2} n_L \epsilon_0 c \int_{A_{\text{eff}}} |E(t)|^2 dA_{\text{eff}} \\ &\equiv \frac{1}{2} n_L \epsilon_0 c A_{\text{eff}} \left( |E_P|^2 + |E_L|^2 + 2\Re [E_P E_L^* e^{j\Delta\omega t}] \right), \end{aligned} \quad (20)$$

where  $A_{\text{eff}}$  is the effective area [7] and  $\Delta\omega = \omega_P - \omega_L$  denotes the optical beat frequency close to the RF intermediate frequency. Let  $R_{\text{pd}}$  denote the PD responsivity (with units of A/W). The resultant photocurrent is

$$\begin{aligned} i(t) &= R_{\text{pd}} P_{\text{opt}}(t) = \underbrace{\frac{1}{2} n_L \epsilon_0 c R_{\text{pd}} A_{\text{eff}} \left( |E_P|^2 + |E_L|^2 \right)}_{I_{\text{DC}}} \\ &\quad + \underbrace{R_{\text{pd}} n_L \epsilon_0 c A_{\text{eff}} \Re [E_P E_L^* e^{j\Delta\omega t}]}_{I_{\text{AC}}(t)}, \end{aligned} \quad (21)$$

where  $I_{\text{DC}}$  collects the slowly varying terms and  $I_{\text{AC}}$  captures the heterodyne beat current. For notational simplicity, we define a constant  $\kappa \equiv n_L \epsilon_0 c A_{\text{eff}}$  having units of  $[\text{W} \cdot \text{m}^2/\text{V}^2]$ . Substituting  $E_L$  into the beat-current expression yields the frequency-domain baseband current

$$i(\omega) = R_{\text{pd}} \kappa E_P G_{\text{opt}}(\omega) E_{\text{RF}}(\omega). \quad (22)$$

Finally, the photocurrent passes through a transimpedance amplifier or low-noise amplifier (LNA) having a gain of  $G_{\text{LNA}}$ , resulting in the receiver output voltage

$$y(\omega) = G_{\text{LNA}} R_{\text{pd}} \kappa E_P G_{\text{opt}}(\omega) E_{\text{RF}}(\omega) + n(\omega), \quad (23)$$

where  $n(\omega)$  represents the aggregate baseband noise observed at the receiver output. It is comprised of contributions from several physical mechanisms, such as blackbody-radiation (BBR)-induced external noise, photon shot noise (PSN) associated with the probe and generated optical fields, quantum projection noise (QPN), PD noise, and so on. A detailed noise budget for SWM-based Rydberg atomic receivers follows directly from the modeling framework in our earlier work [7]. In the present paper, our primary focus is on the bandwidth characteristics of the SWM-based architecture. Therefore, we do not further elaborate on these noise terms and treat  $n(\omega)$  as an effective additive noise process.

### III. PERFORMANCE ANALYSIS

Given the baseband signal model presented in (23), the key performance metrics of interest are the available 3-dB bandwidth and the linear dynamic range of the SWM-based Rydberg atomic receiver. Since the optical and electronic stages are designed to be nearly flat over the frequency region of interest, the overall RF bandwidth is essentially determined by the atomic response embedded in  $G_{\text{opt}}$ . In the following, we first identify how the six-level SWM process gives rise

to an effective two-pole low-pass response that sets the 3-dB bandwidth. Based on this understanding, we then discuss the linear dynamic range and the trade-offs between bandwidth and nonlinearity for the proposed SWM architecture.

#### A. 3-dB Bandwidth Analysis

According to the system model established in Sec. II, the transfer function from the RF Rabi frequency  $\Omega_{\text{RF}}$  to the optical readout  $\rho_{61}(\omega)$  can be expressed as

$$\frac{\rho_{61}(\omega)}{\Omega_{\text{RF}}(\omega)} = \left(\frac{j}{2}\right)^5 \frac{\Omega_P \Omega_C \Omega_{\text{LO}} \Omega_A^*}{D_2 D_3 D_4 \left[ D_5(\omega) D_6(\omega) + \frac{|\Omega_A|^2}{4} \right]}, \quad (24)$$

where the factors  $D_2 D_3 D_4$  are nearly independent of  $\omega$  over the frequency range of interest, so they can be treated as a constant gain. The frequency-selective part of the response is therefore entirely contained in the term

$$H(\omega) \propto \frac{1}{D_5(\omega) D_6(\omega) + \frac{|\Omega_A|^2}{4}}, \quad (25)$$

which represents an effective second-order low-pass filter. For a more intuitive exposition, we focus on operation near the optimal working point, where the RF is close to two-photon resonance with the LO and auxiliary field (i.e.,  $\Delta_{51} \approx \Delta_{61} \approx 0$ ). By writing complex frequency as  $s = j\omega$ , the denominator of  $H(\omega)$  can be restructured into a standard second-order form

$$D_5(\omega) D_6(\omega) + \frac{|\Omega_A|^2}{4} = (s - \lambda_+) (s - \lambda_-), \quad (26)$$

with two poles  $\lambda_{\pm}$  given by

$$\lambda_{\pm} = -\frac{\gamma_{51} + \gamma_{61}}{2} \pm \frac{1}{2} \sqrt{(\gamma_{51} - \gamma_{61})^2 - |\Omega_A|^2}. \quad (27)$$

The real parts of these poles control how fast the RF-induced excitation decays in time. We therefore define the corresponding decay rates

$$\gamma_{\pm} \equiv -\Re \{\lambda_{\pm}\}, \quad (28)$$

which have units of rad/s. Intuitively,  $\gamma_-$  characterizes the slow mode (longer-lived response) and  $\gamma_+$  captures the fast mode. Note that the physical meaning of  $\gamma_{\pm}$  is not the optical linewidth in the sense of FWHM. Instead, they represent the inverse time constants, or equivalently, the half-power angular frequencies of two effective first-order modes that together constitute the overall second-order response. In the overdamped regime  $\Omega_A < |\gamma_{51} - \gamma_{61}|$ , both  $\lambda_+$  and  $\lambda_-$  are real and negative, so the SWM chain behaves as a monotonic two-pole low-pass system.

Then, normalizing the optical transfer function to its DC gain, the magnitude response can be given by

$$\frac{|G_{\text{opt}}(j\omega)|^2}{|G_{\text{opt}}(0)|^2} = \frac{1}{(1 + \omega^2/\gamma_+^2)(1 + \omega^2/\gamma_-^2)}. \quad (29)$$

The 3-dB bandwidth  $\omega_{3\text{dB}}$  is defined by the condition

$$\frac{|G_{\text{opt}}(j\omega_{3\text{dB}})|^2}{|G_{\text{opt}}(0)|^2} = \frac{1}{2}, \quad (30)$$

which leads to

$$\left[1 + \left(\frac{\omega_{3dB}}{\gamma_+}\right)^2\right] \left[1 + \left(\frac{\omega_{3dB}}{\gamma_-}\right)^2\right] = 2. \quad (31)$$

Solving this quadratic equation yields a closed-form expression

$$\omega_{3dB}^2 = \frac{-(\gamma_+^2 + \gamma_-^2) + \sqrt{(\gamma_+^2 + \gamma_-^2)^2 + 4\gamma_+^2\gamma_-^2}}{2}. \quad (32)$$

**Remark 1.** The result in (32) provides some clear insights in several limiting cases as follows.

- 1) When the two levels  $|5\rangle$  and  $|6\rangle$  have comparable dephasing rate,  $\gamma_{51} \approx \gamma_{61} \approx \gamma$ , the two poles merge and the system behaves like a critically damped two-pole low-pass filter. In this case, we have  $\gamma_+ \approx \gamma_- \approx \gamma$ , the magnitude response reduces to

$$\frac{|G_{opt}(\omega)|^2}{|G_{opt}(0)|^2} \approx \frac{1}{(1 + \omega^2/\gamma^2)^2}. \quad (33)$$

Then, the 3-dB bandwidth is given by

$$\omega_{3dB} = \gamma\sqrt{\sqrt{2} - 1} \approx 0.644\gamma. \quad (34)$$

- 2) If one mode decays much more slowly than the other, e.g.,  $\gamma_- \ll \gamma_+$ , the slow pole dominates the roll-off. The second factor in the denominator remains close to unity over the relevant range and the response is effectively first order, so that the 3-dB bandwidth becomes

$$\omega_{3dB} \approx \gamma_-. \quad (35)$$

- 3) When the auxiliary Rabi frequency is large enough that  $|\Omega_A| \gtrsim |\gamma_{61} - \gamma_{51}|$ , the two decay rates converge towards their average value, i.e.,  $\gamma_{\pm} \rightarrow \frac{\gamma_{51} + \gamma_{61}}{2}$ . Substituting this into the equal-rate result yields

$$\omega_{3dB} \approx 0.644 \frac{\gamma_{51} + \gamma_{61}}{2}. \quad (36)$$

This reveals that, by increasing  $\Omega_A$  into the strong-coupling regime, the SWM configuration can push the 3-dB bandwidth up to a value on the order of the average decoherence rate of the last two levels, despite each individual level still being subject to its own dephasing. In other words, provided that  $\Omega_A$  is chosen on the order of or larger than  $|\gamma_{61} - \gamma_{51}|$ , a substantial broadening of the receiver bandwidth can be achieved.

## B. Sensitivity Analysis

We now quantify the electric-field sensitivity of the SWM-based Rydberg atomic receiver. To place different noise sources on a common footing, we adopt the noise-equivalent field (NEF) [21], [32]. NEF is defined as the minimum input RF field amplitude that yields an output SNR = 1 over an effective noise bandwidth  $B^1$ :

$$\text{NEF} \triangleq \frac{|E_{RF}|_{\min}}{\sqrt{B}} \left( \text{V/m}/\sqrt{\text{Hz}} \right), \quad (37)$$

<sup>1</sup>Here,  $B$  denotes the measurement (or noise-equivalent) bandwidth used to integrate noise power, i.e., the effective bandwidth of the baseband filtering employed in the sensitivity readout. It is therefore not necessarily identical to the receiver's small-signal 3-dB bandwidth characterized by  $\omega_{3dB}$ . For a fair, order-of-magnitude sensitivity evaluation and for comparing different receiver configurations under the same full-passband operation, we may choose  $B \approx f_{3dB}$ .

where  $|E_{RF}|_{\min}$  denotes the minimum detectable field.

We then investigate the noise sources and their NEFs, considering one extrinsic contribution (free-space BBR noise) and several intrinsic contributions, in which each term is expressed as a NEF referred to the RF input.

- **Extrinsic Noise Induced by Black-Body Radiation (BBR):** As established in our prior work [7], the external field noise floor NEF<sub>ex</sub> is modeled as

$$\text{NEF}_{\text{ex}} = \sqrt{\frac{16\pi f_{\text{RF}}^2}{3\epsilon_0 c^3} \Theta(f_{\text{RF}}, T)}, \quad (38)$$

where  $\Theta(f_{\text{RF}}, T)$  represents a modified version of the Callen-Welton law [33],  $T$  denotes the ambient physical temperature,  $f_{\text{RF}}$  is the RF signal frequency,  $\epsilon_0$  is the vacuum permittivity, and  $c$  is the speed of light.

- **Quantum Projection Noise (QPN):** For an ensemble of  $N_{\text{atoms}}$  atoms, the SQL-limited field noise is given by

$$\text{NEF}_{\text{QPN}} = \frac{\hbar}{\wp_{\text{RF}} \sqrt{N_{\text{atoms}} T_2}}, \quad (39)$$

where  $\wp_{\text{RF}}$  represents the RF dipole matrix element and  $T_2$  is the coherence time of the SWM process.

- **Photon Shot Noise (PSN):** From (21), the DC photocurrent  $I_{\text{DC}}$  can be readily obtained. The corresponding power spectral density of PSN is given by  $2eI_{\text{DC}}$ , where  $e$  denotes the elementary charge. Referring this noise back to the SWM system's RF input yields

$$\text{NEF}_{\text{PSN}} = \frac{\sqrt{2eI_{\text{DC}}}}{R_{\text{pd}}\kappa E_{\text{P}} |G_{\text{opt}}(0)|}. \quad (40)$$

- **Laser Relative Intensity Noise (RIN):** RIN characterizes classical amplitude fluctuations of the laser power. In the optical power domain, the power spectral density, denoted by  $S_{P,\text{RIN}}$ , is given by

$$S_{P,\text{RIN}} = |\bar{P}_{\text{opt}}|^2 S_{\text{RIN}}, \quad (41)$$

where  $\bar{P}_{\text{opt}}$  takes the average optical power incident on the photodetector (i.e.,  $P_{\text{out}}(t)$  in (20)). When expressed in the photocurrent domain, the power spectral density, denoted by  $S_{i,\text{RIN}}$ , is in the form of

$$S_{i,\text{RIN}} = R_{\text{pd}}^2 |\bar{P}_{\text{opt}}|^2 S_{\text{RIN}}. \quad (42)$$

We then obtain the RF-input-referred NEF

$$\text{NEF}_{\text{RIN}} = \frac{|\bar{P}_{\text{opt}}| \sqrt{S_{\text{RIN}}}}{\kappa E_{\text{P}} |G_{\text{opt}}(0)|}. \quad (43)$$

In practice,  $S_{\text{RIN}}$  can be taken from datasheets [34], [35] or measured.

- **Thermal Noise (TN):** The spectral power of TN over bandwidth  $B$  is modeled as

$$S_{\text{TN}} = \begin{cases} 4k_{\text{B}}TB, & \text{TIA front-end,} \\ Fk_{\text{B}}TB, & \text{LNA front-end,} \end{cases} \quad (44)$$

where  $F$  is the noise factor. By referring this voltage noise to the RF input, we arrive at the noise field given by

$$\text{NEF}_{\text{TN}} = \frac{\sqrt{S_{\text{TN}}}}{G_{\text{LNA}} R_{\text{pd}} \kappa E_{\text{P}} |G_{\text{opt}}(0)|}. \quad (45)$$

Then, the above noise contributions are independent and combine in quadrature:

$$\text{NEF}_{\text{tot}}^2 = \text{NEF}_{\text{ex}}^2 + \text{NEF}_{\text{QPN}}^2 + \text{NEF}_{\text{PSN}}^2 + \text{NEF}_{\text{RIN}}^2 + \text{NEF}_{\text{TN}}^2. \quad (46)$$

### C. Linear Dynamic Range

In addition to bandwidth, the receiver has to remain sufficiently linear over an appropriate range of input amplitudes; otherwise, strong signals will induce gain compression or generate in-band distortion that degrades detection and demodulation. For the SWM-based Rydberg atomic receiver, we characterize the linear dynamic range using two widely adopted metrics: P1dB and IIP3, which are briefly summarized as follows.

- **1-dB compression point (P1dB):** P1dB quantifies the onset of saturation under a single-tone excitation. As the input amplitude increases, the output no longer scales proportionally with the input, while the small-signal gain starts to drop. The P1dB point is defined as the input level at which the gain is reduced by 1 dB compared with the extrapolated linear response. In simple terms, a larger P1dB indicates that the receiver preserves linear amplification over a wider input range.

- **Input-referred third-order intercept point (IIP3):** IIP3 quantifies third-order nonlinear distortion under a two-tone excitation. When a pair of closely-spaced tones at  $\omega_1$  and  $\omega_2$  are applied, third-order nonlinearity generates inter-modulation products at  $2\omega_1 - \omega_2$  and  $2\omega_2 - \omega_1$ , which typically fall back into (or near) the signal band and thus are particularly harmful for wideband or multi-carrier signals. A higher IIP3 implies better linearity and weaker in-band third-order inter-modulation distortion (IMD3) for the same input level.

In our atomic system, the “input amplitude” is the RF Rabi frequency  $\Omega_{\text{RF}}$ , which is proportional to the incident RF electric-field amplitude. The “output” can be chosen as  $\rho_{61}(\omega)$  (or equivalently, the detected baseband voltage  $y$ ), because the optical readout and electronic chain are assumed linear and therefore introduce only a constant scaling. With these definitions, we next derive analytical expressions for P1dB and IIP3.

1) *P1dB*: We first consider a single-tone RF drive at angular frequency  $\omega$ . The gain from the RF Rabi frequency to  $\rho_{61}(\omega)$  is defined as

$$G(\omega, \Omega_{\text{RF}}) \equiv \frac{\rho_{61}(\omega)}{\Omega_{\text{RF}}}. \quad (47)$$

When the nonlinearity is weak, the response of the SWM chain to the RF amplitude can be written as a third-order power series, which is given by

$$\rho_{61}(\omega) \approx H_1(\omega) \Omega_{\text{RF}} + \frac{3}{4} H_3(\omega) \Omega_{\text{RF}}^3, \quad (48)$$

where  $H_1(\omega)$  and  $H_3(\omega)$  are frequency-dependent coefficients that describe the linear and cubic response of the atomic system, respectively. Then, the gain in (47) can be recast as

$$G(\omega, \Omega_{\text{RF}}) \approx H_1(\omega) \left[ 1 + \frac{3}{4} \frac{H_3(\omega)}{H_1(\omega)} \Omega_{\text{RF}}^2 \right]. \quad (49)$$

For most operating points of interest, the real part of  $H_3(\omega)/H_1(\omega)$  is negative, corresponding to gain saturation. We define

$$\alpha(\omega) \equiv \Re \left\{ \frac{H_3(\omega)}{H_1(\omega)} \right\} < 0. \quad (50)$$

Normalizing to the gain  $G(\omega, 0) = H_1(\omega)$  and linearizing the magnitude for  $\Omega_{\text{RF}}$ , we obtain

$$\frac{G(\omega, \Omega_{\text{RF}})}{G(\omega, 0)} \approx 1 + \frac{3}{4} \alpha(\omega) \Omega_{\text{RF}}^2. \quad (51)$$

The P1dB is defined as the input level  $\Omega_{\text{P1dB}}$  at which the gain drops by 1 dB relative to the small-signal value:

$$\begin{aligned} 20 \log_{10} \frac{|G(\omega, \Omega_{\text{P1dB}})|}{|G(\omega, 0)|} &= -1 \text{ dB} \\ \Rightarrow \frac{G(\omega, \Omega_{\text{P1dB}})}{G(\omega, 0)} &\approx 1 + \frac{3}{4} \alpha(\omega) \Omega_{\text{P1dB}}^2 = 10^{-\frac{1}{20}}. \end{aligned} \quad (52)$$

Solving for  $\Omega_{\text{P1dB}}$  yields

$$\Omega_{\text{P1dB}}(\omega) \approx \sqrt{\frac{4}{3} \frac{10^{-1/20} - 1}{\alpha(\omega)}}, \alpha(\omega) < 0. \quad (53)$$

This expression explicitly reveals how the third-order coefficient  $H_3(\omega)$ , through  $\alpha(\omega)$ , controls the onset of gain compression: a smaller  $\alpha(\omega)$  corresponds to a larger the P1dB and, consequently, an expanded linear input range.

2) *IIP3*: To characterize the receiver linearity under multi-tone or modulated RF signals, we next consider a standard two-tone test. The RF Rabi frequency is taken as an equal-amplitude two-tone signal  $\Omega_{\text{RF}}(t) = \Omega \cos \omega_1 t + \Omega \cos \omega_2 t$ , with  $\omega_1$  and  $\omega_2$  chosen close to each other and within the signal band. Substituting this drive into the third-order expansion in (48) and keeping terms up to third order, we obtain the components of  $\rho_{61}(\omega)$  at the fundamental and third-order inter-modulation frequencies. Specifically, at the fundamental frequency  $\omega_1$ , the response is given by

$$\rho_{61}(\omega_1) \approx H_1(\omega) \Omega_{\text{RF}} + \frac{3}{4} H_3(\omega) \Omega_{\text{RF}}^3, \quad (54)$$

while at the third-order inter-modulation frequency  $2\omega_1 - \omega_2$ , we have

$$\rho_{61}(2\omega_1 - \omega_2) \approx \frac{3}{4} H_3(\omega) \Omega_{\text{RF}}^3. \quad (55)$$

The IMD3 level (in dBc) is defined as the ratio between the intermodulation tone and the fundamental tone at the same output node:

$$\text{IMD3 (dBc)} = 20 \log_{10} \left| \frac{3}{4} \frac{H_3(\omega)}{H_1(\omega)} \Omega_{\text{RF}}^2 \right|. \quad (56)$$

The IIP3 is obtained by extrapolating these two trends and finding their intersection. At the intercept, the magnitude of the fundamental and IMD3 tone are equal, which delivers

$$\begin{aligned} |H_1(\omega)| \Omega_{\text{IIP3}} &\approx \frac{3}{4} |H_3(\omega)| \Omega_{\text{IIP3}}^3 \\ \Rightarrow \Omega_{\text{IIP3}}(\omega) &\approx \sqrt{\frac{4}{3} \left| \frac{H_1(\omega)}{H_3(\omega)} \right|}. \end{aligned} \quad (57)$$

A higher IIP3 means that the third-order distortion remains much smaller than the desired signal over a wider input range, which is particularly important for wideband or multi-carrier RF operation. Together with the P1dB analyses above,

the expression for both  $\Omega_{\text{P1dB}}$  and  $\Omega_{\text{IIP3}}$  provide a compact characterization of the linear dynamic range of the SWM-based Rydberg atomic receiver, and make clear how it is determined by the frequency-dependent coefficients  $H_1(\omega)$  and  $H_1(\omega)$  of the underlying atomic response.

#### IV. SIMULATION RESULTS

##### A. Parameter Configuration

We numerically evaluate the six-level SWM-based Rydberg atomic receiver by employing the QuTiP toolkit [31], where the parameters are taken from [27], [28] to ensure physical plausibility. Specifically, energy levels of a  $^{87}\text{Rb}$  atom coupled by six nearly-resonant optical field are given by:  $|1\rangle = |5S_{1/2}, F = 2, m_F = 2\rangle$ ,  $|2\rangle = |5P_{3/2}, F = 3, m_F = 3\rangle$ ,  $|3\rangle = |30D_{3/2}, m_J = 1/2\rangle$ ,  $|4\rangle = |31P_{3/2}, m_J = 1/2\rangle$ ,  $|5\rangle = |30D_{5/2}, m_J = 1/2\rangle$ , and  $|6\rangle = |5P_{3/2}, F = 2, m_F = 1\rangle$ . The SWM atomic system considered is driven by five near-resonant fields, i.e., probe (P), coupling (C), auxiliary (A), local oscillator (LO), and the RF signal, whose Rabi frequencies are configured as  $\Omega_{\text{P}}/2\pi = 1.14$  MHz,  $\Omega_{\text{C}}/2\pi = 9.0$  MHz,  $\Omega_{\text{A}}/2\pi = 6.2$  MHz,  $\Omega_{\text{LO}}/2\pi = 1.4$  MHz, and  $\Omega_{\text{RF}}/2\pi = 1.0$  MHz, respectively. Accordingly, the coherence dephasing rate  $\gamma_{ij}$  applied can be given by:  $\gamma_{21}/2\pi = 6.1$  MHz,  $\gamma_{31}/2\pi = 50$  kHz,  $\gamma_{41}/2\pi = 80$  kHz,  $\gamma_{51}/2\pi = 129$  kHz, and  $\gamma_{61}/2\pi = 6.1$  MHz. The electric dipole matrix elements of the atomic transitions presented in Fig. 1(a) are, in Hartree atomic units,  $|\mu_{12}| = 2.99$ ,  $|\mu_{23}| = 0.00914$ ,  $|\mu_{34}| = 211$ ,  $|\mu_{45}| = 387$ ,  $|\mu_{56}| = 0.0318$ , and  $|\mu_{61}| = 1.22$ .

In more detail, the atomic cloud is Gaussian distributed, with a  $1/e^2$  radius of 1.85 mm, a peak atomic density of  $N_0 \sim 2 \times 10^{10}$  cm $^{-3}$ , and a temperature of approximately 70  $\mu\text{K}$ . This volume has a diameter of  $\sim 2 \times 25$   $\mu\text{m}$  and a length of  $\sim 2 \times 1.85$  mm. The probe (P), coupling (C), and auxiliary (A) beam lasers are focused onto the atomic cloud with  $1/e^2$  radius of 25  $\mu\text{m}$ , 54  $\mu\text{m}$ , and 45  $\mu\text{m}$ , respectively. The beams for both coupling (C) and auxiliary (A) are derived from a single 482 nm laser, while that of the probe (P) field comes from a 780 nm laser. The laser intensities are approximately 20  $\mu\text{W}$  for the probe and 17 mW for each of the coupling and auxiliary beams. In the microwave domain, the LO and RF fields are applied at  $f_{\text{LO}} = 84.18$  GHz and  $f_{\text{RF}} = 83.72$  GHz, respectively. The remaining parameters are specified as follows:  $\epsilon_0 = 8.854 \times 10^{-12}$  F/m,  $G_{\text{LNA}} = 20$  dB, and  $R_{\text{pd}} = 0.55$  A/W.

##### B. Performance Evaluation

1) *Spectra:  $\rho_{61}$  vs.  $\Delta_{\text{P}}$ :* Fig. 2 characterizes the steady-state SWM response by plotting the normalized readout  $\rho_{61}$  versus the probe detuning  $\Delta_{\text{P}}$ . Fig. 2(a) and Fig. 2(b) compare two detuning scenarios. In Fig. 2(a), all optical and RF fields remain close to their multi-photon resonance conditions, so the six-level excitation pathway that generates the SWM procedure is efficient over a wide range of  $\Delta_{\text{P}}$ . This corresponds to an amplitude FWHM of 11.21 MHz. Because the curves in Fig. 2 are plotted in terms of normalized amplitude, the 3-dB bandwidth (defined at half the maximum power) is measured at the points where the normalized amplitude satisfies  $|\rho_{61}| = |\rho_{61}|_{\text{max}}/\sqrt{2}$ , so this FWHM is numerically

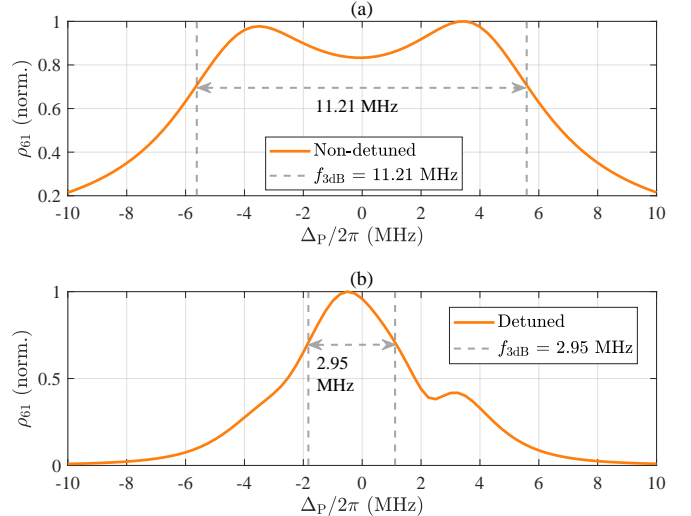


Fig. 2. Normalized steady-state solution  $\rho_{61}$  versus the probe detuning  $\Delta_{\text{P}}$ .

equal to the 3-dB bandwidth. In the following, we refer to this quantity as the 3-dB bandwidth  $f_{3\text{dB}}$ . By contrast, in the case of detunings shown in Fig. 2(b), as  $\Delta_{\text{P}}$  moves away from zero, the multi-photon resonance rapidly degrades, producing an asymmetric, much narrower line with  $f_{3\text{dB}} = 2.95$  MHz.

Fig. 3 visualizes the normalized steady-state solution  $\rho_{61}$  as the probe detuning  $\Delta_{\text{P}}$  is swept along with different Rabi frequencies. The main trends in Fig. 3, which elaborates their rationales and engineering implications, highlighting how each control field affects the 3-dB bandwidth and suggests which parameters are most suitable for engineering wideband SW-based Rydberg atomic receivers.

2) *3-dB Bandwidth vs.  $\Omega_A$ :* Fig. 4 portrays the atomic system response from the input  $\Omega_{\text{RF}}$  to the optical output,  $\rho_{41}$  for the four-level EIT scheme and  $\rho_{61}$  for six-level SWM scheme. For each architecture, Liouvillian master equation is linearized around the steady state and the atomic system response (i.e., the frequency-domain transfer function) is computed from the RF Rabi-frequency  $\Omega_{\text{RF}}$  to the optical output. The plotted magnitude responses correspond to  $|H(\omega)|$ , normalized to their respective low-frequency values  $|H(0)|$ , such that both curves start at 0 dB and can be compared on the same scale. The horizontal dashed line marks the 3-dB bandwidth. As illustrated in Fig. 4, the EIT scheme exhibits typical low-pass characteristics, whose normalized gain remains flat only up to a few hundred kilohertz and then rolls off steadily, crossing the -3 dB level at  $f_{3\text{dB}} \approx 0.66$  MHz. By contrast, the 3-dB bandwidth achieved by the SWM scheme is  $f_{3\text{dB}} \approx 7.2$  MHz, more than an order of magnitude larger than that of the EIT counterpart given the same optical driven levels.

Fig. 5 depicts how the 3-dB bandwidth  $f_{3\text{dB}}$  varies with Rabi frequencies  $\Omega_{\text{LO}}$ ,  $\Omega_{\text{A}}$ , and  $\Omega_{\text{RF}}$ . The 3-dB bandwidth  $f_{3\text{dB}}$  is defined as the frequency where  $|H(\omega)|$  first drops to  $|H(0)|/\sqrt{2}$ . More specifically, Fig. 5(a) shows that the 3-dB bandwidth first increases and then decreases with  $\Omega_{\text{LO}}$ . This behavior can be understood by examining how the SWM lock-in spectrum evolves with probe detuning  $\Delta_{\text{P}}$ . For small  $\Omega_{\text{LO}}$ , the transition  $|3\rangle \rightarrow |4\rangle$  is only weakly dressed and

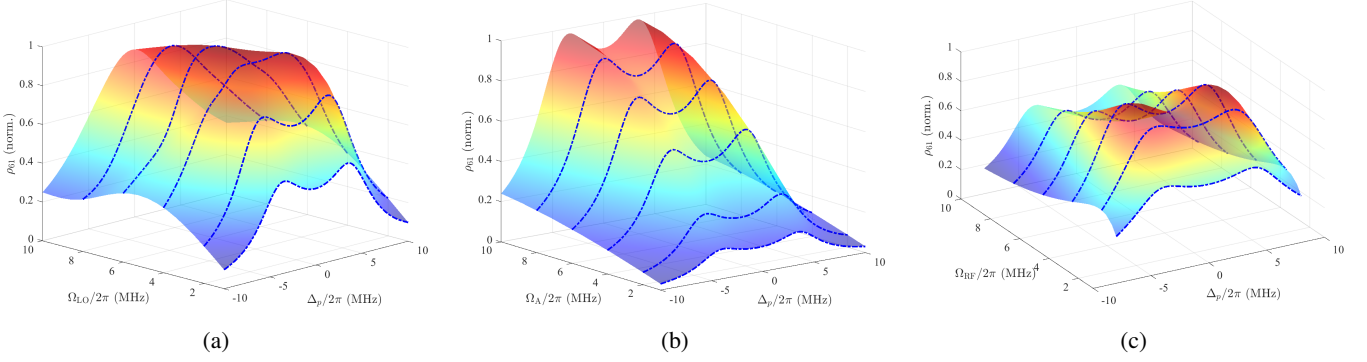


Fig. 3. Dependence of normalized steady-state solution  $\rho_{61}$  on Rabi frequencies: (a)  $\Omega_{LO}$ , (b)  $\Omega_A$ , and (c)  $\Omega_{RF}$ .

TABLE I. Main trends in Fig. 3 and their rationales along with engineering implications.

Rabi frequency	Trend of $\rho_{61}$	3-dB bandwidth behavior	Rationale	Engineering implication
$\Omega_{LO}$ (Fig. 3(a))	Curves first broaden, then become more single-peaked and steeper at the edges when $\Omega_{LO}$ is large	Bandwidth increases for small-moderate $\Omega_{LO}$ , then decreases for large $\Omega_{LO}$ (non-monotonic)	Moderate LO dressing opens additional paths and power-broadens the response; very strong LO pulls the dressed resonances together and compresses the wings	$\Omega_{LO}$ must be chosen in an intermediate range; too small wastes bandwidth, too large reduces the effective bandwidth
$\Omega_A$ (Fig. 3(b))	Curves expand almost uniformly with $\Omega_A$ ; peak position stays nearly fixed	Bandwidth grows roughly monotonically with $\Omega_A$	Stronger auxiliary coupling enhances extraction and overall SWM gain, so a wider range of $\Delta_p$ still gives a strong signal	$\Omega_A$ is an efficient and predictable “bandwidth knob” for SWM, easy to tune in practice
$\Omega_{RF}$ (Fig. 3(c))	Peak amplitude increases, but curves become more concentrated around the center	Bandwidth decreases monotonically with $\Omega_{RF}$ at higher drive	Large RF modulation pushes more power into higher harmonics; the first-harmonic component we demodulate becomes spectrally narrower	RF amplitude should be kept in a moderate regime; bandwidth shaping should rely on optical/LO fields rather than on $\Omega_{RF}$

the SWM lock-in signal is determined by a single resonance near  $\Delta_p = 0$ . Increasing  $\Omega_{LO}$  in this regime mixes  $|3\rangle$  and  $|4\rangle$ , increases dephasing rates of levels  $|2\rangle$ ,  $|3\rangle$ , and  $|4\rangle$ , as well as power-broadens this central feature. As a result,  $f_{3dB}$  increase as  $\Omega_{LO}$  is raised. Furthermore, once  $\Omega_{LO}$  grows larger than the homogeneous linewidths of levels  $|3\rangle$  and  $|4\rangle$ , the transition  $|3\rangle \rightarrow |4\rangle$  enters a well-resolved AT regime. The lock-in spectrum then splits two separated lobes, with a pronounced dip around  $\Delta_p = 0$ . Because the FWHM is defined with respect to this central region, the two peaks move apart and the response near  $\Delta_p = 0$  becomes flatter. This induces  $f_{3dB}$  to decrease at large  $\Omega_{LO}$ , even though each individual dressed line is still power-broadened. In short, strong LO dressing redistributes the SWM response into two well-resolved dressed resonances whose contributions partially cancel, effectively re-narrowing the effective spectral window.

Fig. 5(b) demonstrates that increased  $\Omega_A$  leads to a nearly monotonic growth of  $f_{3dB}$ . Here  $\Omega_A$  mainly acts as an additional coupled light field that shortens the effective lifetime of the slow SWM coherence. As a result, the atomic system responds more quickly to the RF signal input. Fig. 5(c) plots  $f_{3dB}$  versus the RF signal intensity, characterized by its Rabi frequency  $\Omega_{RF}$ . As  $\Omega_{RF}$  grow, the transition  $|4\rangle \rightarrow |5\rangle$  is increasingly dressed, while its AC-Stark shift and splitting move the optimal SWM operating point away from exact resonance. As a result, the lock-in lineshape around the operating detuning becomes much flatter and a small RF-induced perturbation produces a smaller change in the detected coherence. This directly reduces the baseband responsivity  $|H(0)|$  and thus the 3-dB bandwidth  $f_{3dB}$  degrades.

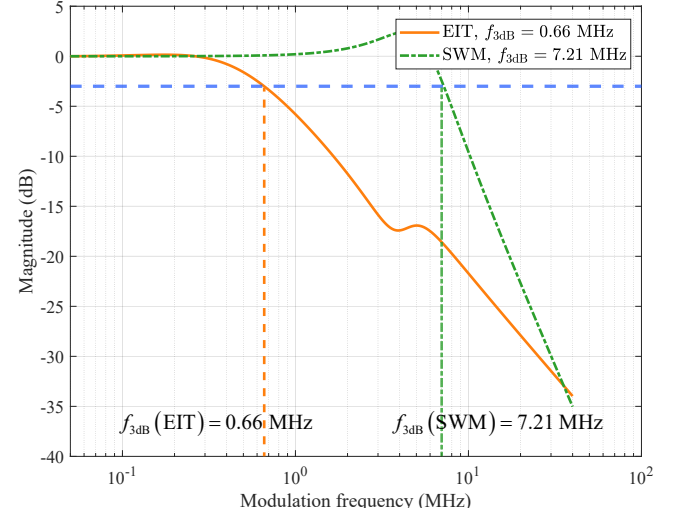


Fig. 4. Atomic system response  $|H(\omega)|$  from the input  $\Omega_{RF}$  to the optical output,  $\rho_{41}$  for EIT and  $\rho_{61}$  for SWM.

Fig. 6 illustrates the baseband response  $|H(0)|$  versus the 3-dB bandwidth  $f_{3dB}$  for both EIT and SWM schemes. For the SWM scheme, sweeping  $\Omega_A$  produces a single-peaked behavior: starting from an under-coupled ladder system,  $|H(0)|$  increases as  $\Omega_A$  strengthens the projection of the RF drive onto the slow dressed mode, but decreases at larger  $\Omega_A$  due to power broadening and AT splitting, both of which increase dephasing rates. As a result, the bandwidth increases monotonically. For EIT sweeping  $\Omega_{LO}$  yields a roughly monotonic decrease in  $|H(0)|$  as the bandwidth increases,

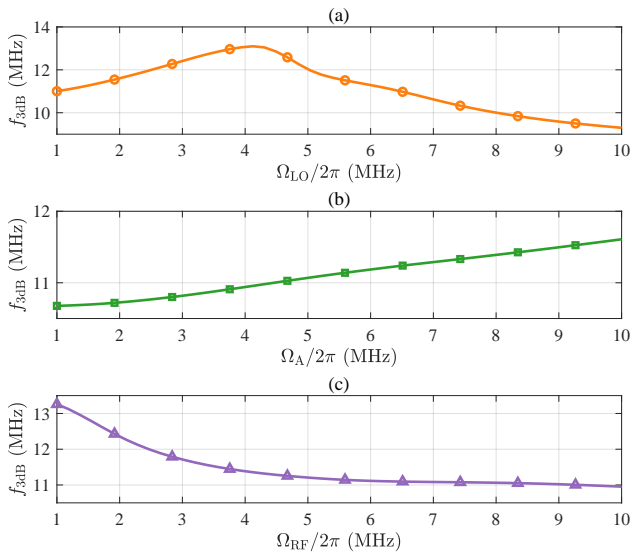


Fig. 5. Dependence of the 3-dB bandwidth on the (a) LO Rabi frequency  $\Omega_{LO}$ , (b) auxiliary Rabi frequency  $\Omega_A$ , and (c) RF Rabi frequency  $\Omega_{RF}$  in the SWM-based atomic system.

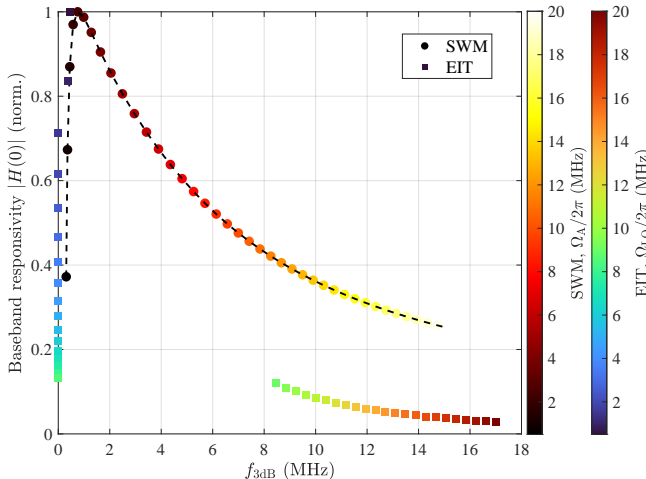


Fig. 6. Baseband response  $|H(0)|$  versus the 3-dB bandwidth  $f_{3dB}$  for EIT and SWM Rydberg atomic receivers.

reflecting coupling-induced broadening. At a fixed  $f_{3dB}$ , a larger  $|H(0)|$  is desirable, since it corresponds to a stronger baseband respond. In this regard, SWM provides a near-critical-coupling region in which  $|H(0)|$  remains relatively high at moderate bandwidth, whereas EIT tends to exchange increased bandwidth for reduced  $|H(0)|$ .

3) *Sensitivity*: To quantify the electric-field sensitivity of the SWM-based Rydberg atomic receiver in a communication-relevant manner, we adopt the NEF framework as presented in (46). Fig. 8 plots the NEF as a function of the baseband frequency. For each frequency, we extract the small-signal transduction gain from the RF field to the detected voltage by demodulating the simulated coherence, and then refer each noise contribution back to the RF input. As observed, at low baseband frequency, the receiver exhibits a near-constant sensitivity, where  $NEF_{tot}$  is

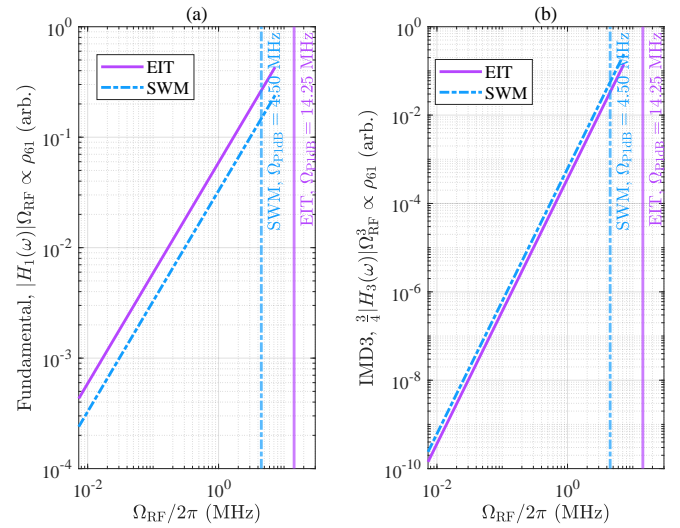


Fig. 7. (a) Fundamental components versus the RF Rabi frequency  $\Omega_{RF}$ . (b) IMD3 components versus  $\Omega_{RF}$ .

bounded between the BBR floor and the SQL floor, indicating that the system operates in a regime where technical readout noises (PSN/RIN/TN) are sufficiently suppressed and the residual limitation is primarily due to fundamental atomic/environmental noise. As the baseband frequency increases,  $NEF_{PSN}$ ,  $NEF_{RIN}$ , and  $NEF_{TN}$  rise rapidly, leading to a pronounced degradation of  $NEF_{tot}$ . This trend is not only due to an intrinsic increase of these noise sources themselves, but rather attributes to the  $NEF_{tot}$  with frequency. More specifically, when the effective RF-to-optical conversion magnitude decreases, the same detection-chain noise corresponds to a larger input-referred field. Furthermore, the 3-dB bandwidth is  $f_{3dB} = 7.21$  MHz, beyond which the sensitivity penalty becomes increasingly severe.

Fig. 9(a) demonstrates the tradeoff behaviors when sweeping the Rabi frequency of the auxiliary field  $\Omega_A$ . As it transpires, increasing  $\Omega_A$  substantially extends the 3-dB bandwidth  $f_{3dB}$  but at the cost a gradually higher NEF, i.e., degraded sensitivity. This trend is consistent with a gain–bandwidth trade-off: stronger auxiliary coupling accelerates the SWM dynamics and shifts the effective pole to higher frequencies, while simultaneously reducing the low-frequency conversion efficiency, thus increasing the input-referred impact of readout-chain noises. By contrast, Fig. 9(b) presents the tradeoff analysis when sweeping the LO Rabi frequency  $\Omega_{LO}$  while keeping  $\Omega_A$  fixed. Here,  $f_{3dB}$  remains nearly unchanged and the corresponding NEF varies only marginally. This indicates that  $\Omega_A$  serves as an effective bandwidth knob that determines the sensitivity–bandwidth tradeoff.

### C. Linear Dynamic Range

1) *P1dB and IIP3 Performance*: Fig. 7 and Fig. 10 jointly quantify the third-order nonlinearity of the EIT- and SWM-based Rydberg atomic receivers, while bridging the quantum model to standard RF linearity metric. Taken together, they aim to address two key questions: (i) whether the atomic response behaves as a well-defined third-order nonlinearity

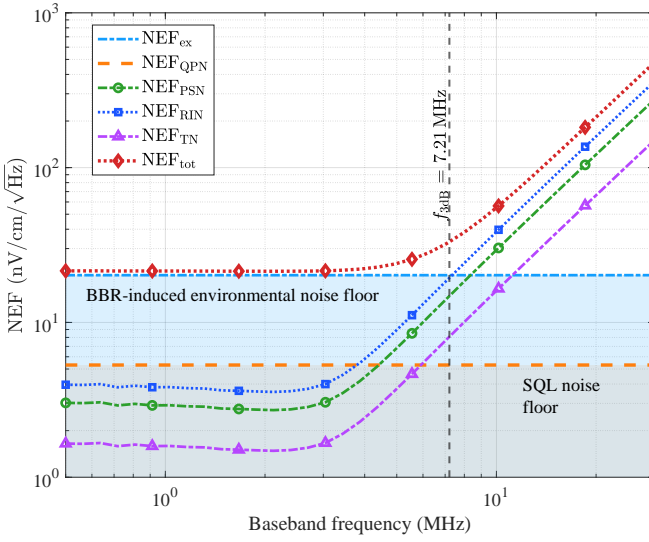


Fig. 8. NEF versus baseband frequency.

over the input range of interest; and (ii) for a given RF driven level, which architecture delivers better multi-tone linearity in terms of conventional IMD3/IIP3 measures.

Fig. 7(a) and (b) illustrate the fundamental component  $H_1(\omega)\Omega_{RF}$  and the IMD3 component  $\frac{3}{4}H_3(\omega)\Omega_{RF}^3$ , respectively, versus the RF Rabi frequency  $\Omega_{RF}$ . The vertical lines in both subfigures mark the P1dB. Specifically, the fundamental component grows with a slope of 1 on the log-log scale in Fig. 7(a), while the IMD3 component follows a slope of approximately of 3 in Fig. 7(b). This confirms that, in the operating region in which we compare both EIT and SWM schemes, the RF response is determined by a third-order nonlinearity, as in classical RF front-ends. Furthermore, for a given  $f_{3dB}$ , the P1dB achieved by the EIT scheme lies at a higher  $\Omega_{RF}$  than that of the SWM counterpart. Again, Fig. 10 re-expressed the same third-order distortion in the RF engineer's language. It plots IMD3 in dBc, defined in (56), versus  $\Omega_{RF}$  on a logarithmic scale. Extrapolating each line to 0 dBc gives the corresponding IIP3, i.e.,  $\Omega_{IIP3}/2\pi = 7.31$  MHz for SWM and  $\Omega_{IIP3}/2\pi = 12.71$  MHz for EIT. The EIT scheme exhibits a higher IIP3 value and thus the wider dynamic linear range.

*Engineering implications.* Fig. 7 and Fig. 10 indicate that both EIT- and SWM-based Rydberg atomic receivers behave as third-order devices whose nonlinearity can be captured by IMD3 and IIP3 metrics. Under the same operation frequency, SWM buys a factor of roughly  $5 \sim 6$  in 3-dB bandwidth compared to EIT, but it pays for the increased bandwidth with a smaller dynamic linear range, i.e., its IMD3 is higher and its IIP3 and P1dB are lower. For system design, this suggests a natural division of operating regimes. The SWM framework is appealing when wide instantaneous bandwidth and multi-tone operation are paramount (where moderate inter-modulation levels can be tolerated), while the EIT framework is better suited to narrowband or channelized links that demand the highest achievable dynamic range.

2) *Trade-off Between Bandwidth and IIP3:* Fig. 11 examines how the RF signal bandwidth and third-order linearity evolve when we tune the key control parameters in a pair

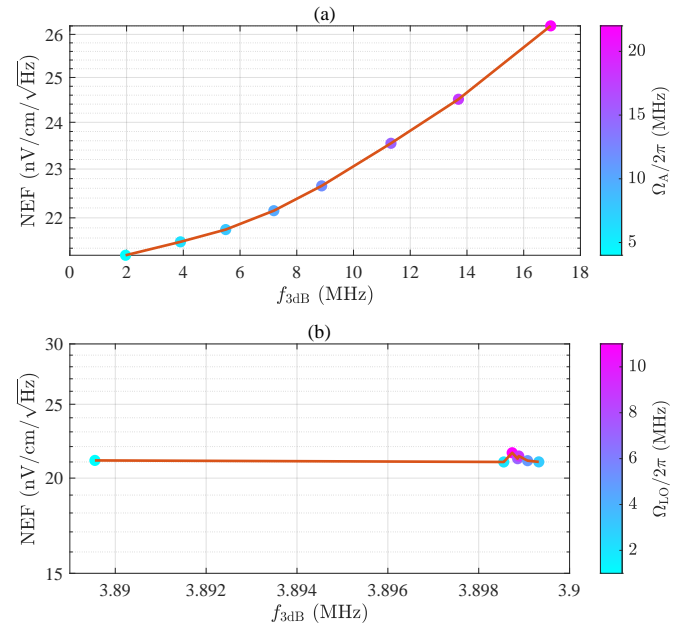


Fig. 9. Tradeoff between NEF and 3-dB bandwidth. (a) Sweeping  $\Omega_A$  with  $\Omega_{LO}$  fixed. (b) Sweeping  $\Omega_{LO}$  with  $\Omega_A$  fixed.

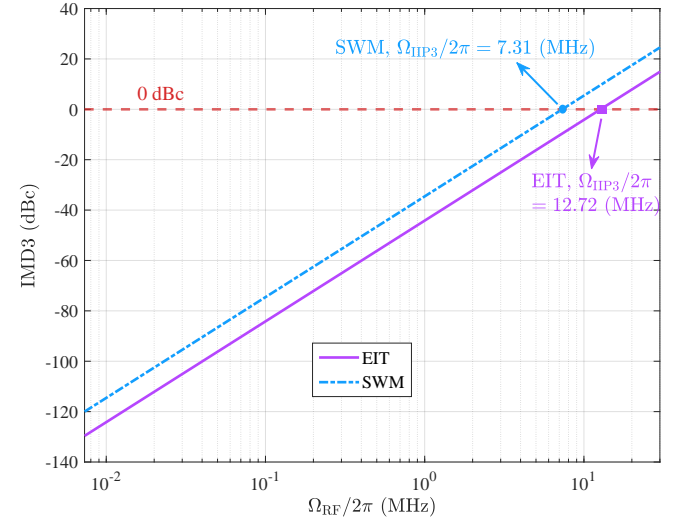


Fig. 10. IMD3 performance in dBc versus the RF Rabi frequency  $\Omega_{RF}$ .

of configurations: the LO Rabi frequency  $\Omega_{LO}$  in the EIT scheme and the auxiliary optical Rabi frequency  $\Omega_A$  in the SWM scheme. Our goal is to identify which knobs can genuinely expand the baseband (envelope) bandwidth, and to what extent this can be achieved without sacrificing input linearity.

In the EIT scheme, as shown in Fig. 11(a) and (c), the solid curve in Fig. 11(a) shows that the low-pass 3-dB bandwidth extracted from the DC components to -3 dB roll-off remains almost flat at a sub-MHz value. As long as  $\Omega_{LO}$  is large enough to dress the  $|3\rangle \rightarrow |4\rangle$  transition, yet not large enough to push the complex poles far away from DC, the DC roll-off is mainly determined by the dephasing rates (e.g.,  $\gamma_{31}, \gamma_{41}$ ) and other additional dephasing channels such as laser linewidth. Consequently,  $f_{3dB}$  hardly changes with

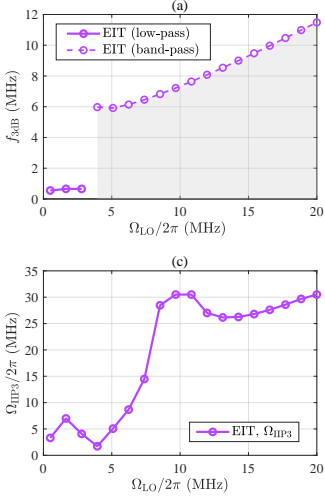


Fig. 11. Dependence of 3-dB bandwidth  $f_{3dB}$  and IIP3 on the Rabi frequencies  $\Omega_{LO}$  and  $\Omega_A$  for EIT and SWM configurations.

$\Omega_{LO}$ . When  $\Omega_{LO}$  is further increased, the system departs from the strict low-pass regime and develops an underdamped resonance: the spectral maximum shifts from DC to a finite frequency, and the dashed curve in Fig. 8(a) tracks the -3 dB point on the high-frequency side of this peak. However, this broadened bandwidth no longer reflects the effective baseband bandwidth. The corresponding IIP3 in Fig. 11(c) exhibits a sharp maximum at a specific  $\Omega_{LO}$ , reflecting near-destructive interference among different RF-induced third-order transition paths at that operating point. Once  $\Omega_{LO}$  deviates from this bias, the cancellation breaks down and the linearity deteriorates rapidly.

As for the SWM scheme shown in Fig. 11(b) and (d), the behavior is much more regular. Over a broad range of  $\Omega_A$ , the response remains strictly low-pass, and the 3-dB bandwidth increases almost linearly with  $\Omega_A$ , as transpired in Fig. 11(b). At the same time, Fig. 8(d) reveals that the IIP3 grows monotonically with  $\Omega_A$ . Physically, the auxiliary field strengthens the desired SWM pathway faster than it enhances the competing higher-order distortion channels, so the ratio  $|H_1(\omega)/H_3(\omega)|$  defined in  $\Omega_{IIP3}$  increases and the useful linear range extends in a smooth manner. From an engineering perspective, this means that SWM provides a robust and easily controllable way to wideband, high-linearity Rydberg reception, while the EIT scheme may be best viewed as a narrowband architecture with a fragile high-linearity sweet spot and, at high  $\Omega_{LO}$ , as a resonant IF readout rather than a truly wideband baseband receiver.

Fig. 12 intends to compare, on the same footing, how much linearity (evaluated by IIP3,  $\Omega_{IIP3}$ ) can be achieved for a given effective 3-dB bandwidth  $f_{3dB}$  when the Rydberg atomic receiver is operated either in a conventional super-heterodyne EIT technique (squares) or in the proposed SWM mode (circles). In other words, it visualizes the design space available to a system engineer: for a target bandwidth, how far can we push the input dynamic range by tuning the driven light field  $\Omega_{LO}$  or  $\Omega_A$ .

Specifically, the SWM points form an almost smooth, rising trend: as  $\Omega_A$  increases, both  $f_{3dB}$  and  $\Omega_{IIP3}$  increase

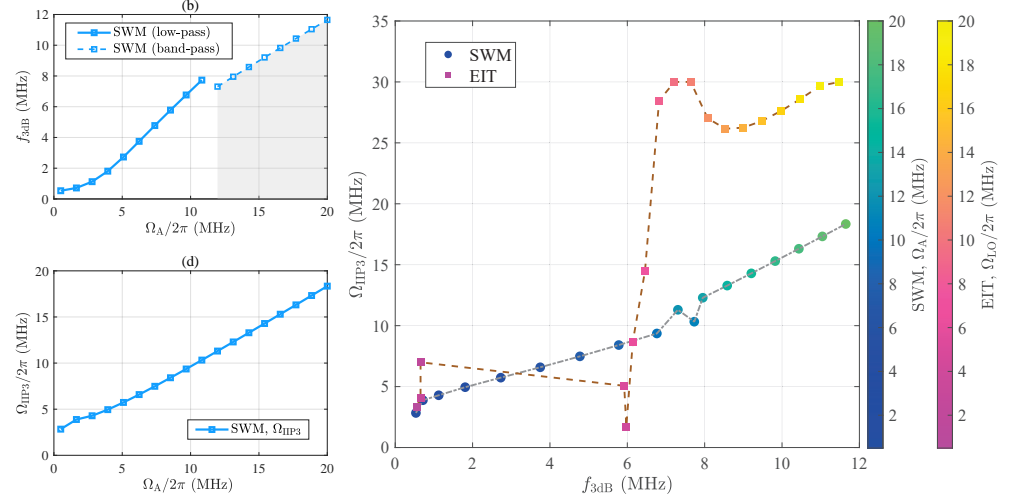


Fig. 12. Trade-off between EIT and SWM schemes with respect to 3-dB bandwidth  $f_{3dB}$  and IIP3  $\Omega_{IIP3}$ .

in a fairly regular way. This indicates a benign bandwidth-linearity relationship for SWM, where moving to a wider bandwidth does not require sacrificing IIP3 within the explored range. Physically,  $\Omega_A$  in the SWM scheme mainly controls the overall strength and power broadening of the SWM pathway: a stronger  $\Omega_A$  enhances the useful third-order susceptibility responsible for detection, while higher-order distortion terms grow more slowly, so the ratio between fundamental and inter-modulation components improves. By contrast, the EIT data exhibits a more structured pattern. For weak  $\Omega_{LO}$ , the system remains narrowband and only moderately linear. As  $\Omega_{LO}$  is increased to approximately 6 MHz, both bandwidth and IIP3 improve; however, beyond this region, the IIP3 shows a pronounced peak followed by a saturation. This can be attributed to interference among multiple RF-induced paths contributing to the third-order response. More explicitly, at a specific  $\Omega_{LO}$ , the third-order distortion components generated along different pathways nearly cancel each other, resulting in a strong suppression of inter-modulation products while the desired linear susceptibility remains large. A slight detuning from this operating point disrupts this cancellation, causing the IIP3 to drop rapidly.

*Engineering implications.* From a practical system design perspective, results in Fig. 11 and Fig. 12 highlight a clear trade-off between linear dynamic range and tunable width. The EIT configuration can deliver exceptionally high IIP3 at a given bandwidth, but only when the LO amplitude and other operating conditions are locked very close to its optimal point. It therefore favors narrowband links or highly controlled laboratory settings where such stabilization is feasible. The SWM configuration, by contrast, provides a more modest IIP3 but delivers a monotonic and predictable trade-off as  $\Omega_A$  is tuned, so its performance is much less sensitive to parameter drift, device non-idealities, or environmental fluctuations. For quantum wireless applications that require wideband operation and long-term stability, this robustness and simple tunability makes SWM particularly attractive, whereas EIT is best reserved for scenarios where the system can be reliably maintained at its fragile high-linearity sweet spot.

## V. CONCLUSION

In this work, we have developed a wideband quantum-transduction framework for a SWM-based Rydberg atomic receiver and established a baseband response model that connects the atomic dynamics to communication-level metrics. Relying upon this model, we analyze the 3-dB baseband bandwidth and derive closed-form expressions that clarify how the bandwidth scales with key optical and RF parameters. We then examine the linear dynamic range, characterized by P1dB and IIP3 metrics. Our analysis and simulation results demonstrate that the SWM configuration supports a broader and more tunable linear region than its EIT counterpart, yielding a smoother and more benign trade-off between bandwidth and linearity. Taken together, these results indicate that SWM-enabled quantum transduction can transform Rydberg atomic receivers from inherently narrowband probes into flexible, wideband front-ends suitable for emerging 6G-oriented sensing and communication applications.

## REFERENCES

- [1] L. Hanzo, Z. Babar, Z. Cai, D. Chandra, I. B. Djordjevic, B. Koczor, S. X. Ng, M. Razavi, and O. Simeone, "Quantum information processing, sensing, and communications: Their myths, realities, and futures," *Proc. IEEE*, to appear, 2025.
- [2] F. Zhang, B. Jin, Z. Lan, Z. Chang, D. Zhang, Y. Jiao, M. Shi, and J. Xiong, "Quantum wireless sensing: Principle, design and implementation," in *Proceedings of the 29th Annual International Conference on Mobile Computing and Networking*, ser. ACM MobiCom '23. New York, NY, USA: Association for Computing Machinery, 2023.
- [3] C. L. Degen, F. Reinhard, and P. Cappellaro, "Quantum sensing," *Rev. Mod. Phys.*, vol. 89, p. 035002, Jul. 2017.
- [4] N. Schlossberger, N. Prajapati, S. Berweger, A. P. Rotunno, A. B. Artusio-Glimpse, M. T. Simons, A. A. Sheikh, E. B. Norrgard, S. P. Eckel, and C. L. Holloway, "Rydberg states of alkali atoms in atomic vapour as SI-traceable field probes and communications receivers," *Nat. Rev. Phys.*, Sep. 2024.
- [5] T. Gong, A. Chandra, C. Yuen, Y. L. Guan, R. Dumke, C. M. S. See, M. Debbah, and L. Hanzo, "Rydberg atomic quantum receivers for classical wireless communication and sensing," *IEEE Wirel. Commun.*, vol. 32, no. 5, pp. 90–100, Oct. 2025.
- [6] M. Cui, Q. Zeng, and K. Huang, "Rydberg atomic receiver: Next frontier of wireless communications," *IEEE Commun. Mag.*, vol. 64, no. 1, pp. 146–152, Jan. 2026.
- [7] Y. Chen, X. Guo, C. Yuen, Y. Zhao, Y. L. Guan, C. M. S. See, M. Débbah, and L. Hanzo, "Harnessing Rydberg atomic receivers: From quantum physics to wireless communications," *arXiv preprint: 2501.11842*, 2025. [Online]. Available: <https://arxiv.org/abs/2501.11842>
- [8] M. Cui, Q. Zeng, and K. Huang, "Towards atomic MIMO receivers," *IEEE J. Sel. Areas Commun.*, vol. 43, no. 3, pp. 659–673, Mar. 2025.
- [9] M. Saffman, T. G. Walker, and K. Mølmer, "Quantum information with Rydberg atoms," *Rev. Mod. Phys.*, vol. 82, pp. 2313–2363, Aug 2010.
- [10] Y. Chen, C. Yuen, D. Arumugam, C. M. S. See, M. Debbah, and L. Hanzo, "Polarization-aware doa detection relying on a single rydberg atomic receiver," *arXiv preprint: 2508.17179*, 2025. [Online]. Available: <https://arxiv.org/abs/2508.17179>
- [11] J. A. Sedlacek, A. Schwettmann, H. Kübler, R. Löw, T. Pfau, and J. P. Shaffer, "Microwave electrometry with Rydberg atoms in a vapour cell using bright atomic resonances," *Nat. Phys.*, vol. 8, no. 11, pp. 819–824, Nov. 2012.
- [12] A. P. Rotunno, C. L. Holloway, N. Prajapati, S. Berweger, A. B. Artusio-Glimpse, R. Brown, M. Simons, A. K. Robinson, B. N. Kayim, M. A. Viray, J. F. Jones, B. C. Sawyer, R. Wyllie, T. Walker, R. W. Ziolkowski, S. R. Jefferts, S. Geibel, J. Wheeler, and E. Imhof, "Investigating electromagnetically induced transparency spectral lineshape distortion due to non-uniform fields in Rydberg-atom electrometry," *J. Appl. Phys.*, vol. 134, no. 8, p. 084401, Aug. 2023.
- [13] Z.-K. Liu, L.-H. Zhang, B. Liu, Z.-Y. Zhang, G.-C. Guo, D.-S. Ding, and B.-S. Shi, "Deep learning enhanced Rydberg multifrequency microwave recognition," *Nat. Commun.*, vol. 13, no. 1, p. 1997, Apr. 2022.
- [14] R. Mao, Y. Lin, A. Zhou, K. Yang, and Y. Fu, "Shortwave ultrahigh-sensitivity Rydberg atomic electric field sensing based on a subminiature resonator," *IEEE Trans. Antennas Propag.*, vol. 72, no. 11, pp. 8165–8172, Nov. 2024.
- [15] J. A. Sedlacek, A. Schwettmann, H. Kübler, and J. P. Shaffer, "Atom-based vector microwave electrometry using Rubidium Rydberg atoms in a vapor cell," *Phys. Rev. Lett.*, vol. 111, p. 063001, Aug 2013.
- [16] Y. Wang, F. Jia, J. Hao, Y. Cui, F. Zhou, X. Liu, J. Mei, Y. Yu, Y. Liu, J. Zhang, F. Xie, and Z. Zhong, "Precise measurement of microwave polarization using a Rydberg atom-based mixer," *Opt. Express*, vol. 31, no. 6, pp. 10449–10457, Mar. 2023.
- [17] A. Chopinaud and J. Pritchard, "Optimal state choice for Rydberg-atom microwave sensors," *Phys. Rev. Appl.*, vol. 16, p. 024008, Aug. 2021.
- [18] M. Cloutman, M. Chilcott, A. Elliott, J. S. Otto, A. B. Deb, and N. Kjærgaard, "Polarization-insensitive microwave electrometry using Rydberg atoms," *Phys. Rev. Appl.*, vol. 21, p. 044025, Apr. 2024.
- [19] V. I. Yudin, A. V. Taichenachev, Y. O. Dudin, V. L. Velichansky, A. S. Zibrov, and S. A. Zibrov, "Vector magnetometry based on electromagnetically induced transparency in linearly polarized light," *Phys. Rev. A*, vol. 82, p. 033807, Sep. 2010.
- [20] K. Cox, V. I. Yudin, A. V. Taichenachev, I. Novikova, and E. E. Mikhailov, "Measurements of the magnetic field vector using multiple electromagnetically induced transparency resonances in rb vapor," *Phys. Rev. A*, vol. 83, p. 015801, Jan. 2011.
- [21] H.-T. Tu, K.-Y. Liao, H.-L. Wang, Y.-F. Zhu, S.-Y. Qiu, H. Jiang, W. Huang, W. Bian, H. Yan, and S.-L. Zhu, "Approaching the standard quantum limit of a Rydberg-atom microwave electrometer," *Sci. Adv.*, vol. 10, no. 51, p. eads0683, Dec. 2024.
- [22] G. Sandidge, G. Santamaria-Botello, E. Bottomley, H. Fan, and Z. Popović, "Resonant structures for sensitivity enhancement of Rydberg-atom microwave receivers," *IEEE Trans. Microwave Theory Tech.*, vol. 72, no. 4, pp. 2057–2066, Apr. 2024.
- [23] M. Jing, Y. Hu, J. Ma, H. Zhang, L. Zhang, L. Xiao, and S. Jia, "Atomic superheterodyne receiver based on microwave-dressed Rydberg spectroscopy," *Nat. Phys.*, vol. 16, no. 9, pp. 911–915, Jun. 2020.
- [24] M. T. Simons, A. H. Haddab, J. A. Gordon, and C. L. Holloway, "A Rydberg atom-based mixer: Measuring the phase of a radio frequency wave," *Appl. Phys. Lett.*, vol. 114, no. 11, p. 114101, Mar. 2019.
- [25] F. Wu, Q. An, Z. Sun, and Y. Fu, "Linear dynamic range of a Rydberg-atom microwave superheterodyne receiver," *Phys. Rev. A*, vol. 107, p. 043108, Apr. 2023.
- [26] Y. Zhang, A. W. Brown, and M. Xiao, "Opening four-wave mixing and six-wave mixing channels via dual electromagnetically induced transparency windows," *Phys. Rev. Lett.*, vol. 99, p. 123603, Sep 2007. [Online]. Available: <https://link.aps.org/doi/10.1103/PhysRevLett.99.123603>
- [27] J. Han, T. Vogt, C. Gross, D. Jaksch, M. Kiffner, and W. Li, "Coherent microwave-to-optical conversion via six-wave mixing in Rydberg atoms," *Phys. Rev. Lett.*, vol. 120, p. 093201, Mar. 2018. [Online]. Available: <https://link.aps.org/doi/10.1103/PhysRevLett.120.093201>
- [28] T. Vogt, C. Gross, J. Han, S. B. Pal, M. Lam, M. Kiffner, and W. Li, "Efficient microwave-to-optical conversion using Rydberg atoms," *Phys. Rev. A*, vol. 99, p. 023832, Feb 2019. [Online]. Available: <https://link.aps.org/doi/10.1103/PhysRevA.99.023832>
- [29] S. Borówka, U. Pylypenko, M. Mazelanik, and M. Parniak, "Continuous wideband microwave-to-optical converter based on room-temperature Rydberg atoms," *Nat. Photonics*, vol. 18, no. 1, pp. 32–38, Oct. 2024.
- [30] S. Borówka, M. Mazelanik, W. Wasilewski, and M. Parniak, "Optically-biased Rydberg microwave receiver enabled by hybrid nonlinear interferometry," *Nat. Commun.*, vol. 16, no. 1, p. 8975, Oct. 2025.
- [31] J. R. Johansson, P. D. Nation, and F. Nori, "QuTiP: An open-source Python framework for the dynamics of open quantum systems," *Comp. Phys. Comm.*, vol. 183, no. 8, pp. 1760–1772, Apr. 2012.
- [32] G. Santamaria-Botello, S. Verploegh, E. Bottomley, and Z. Popovic, "Comparison of noise temperature of Rydberg-atom and electronic microwave receivers," *arXiv preprint: 2209.00908*, 2022. [Online]. Available: <https://arxiv.org/abs/2209.00908>
- [33] H. B. Callen and T. A. Welton, "Irreversibility and generalized noise," *Phys. Rev.*, vol. 83, pp. 34–40, Jul. 1951.
- [34] Thorlabs, Inc., "Low-noise, narrow-linewidth laser system, o-band (1310 nm)," <https://www.thorlabs.com/low-noise-narrow-linewidth-laser-system-o-band-1310-nm>, accessed: 2026-01-28.
- [35] NKT Photonics, "Koheras adjustik and adjustik hp datasheet," NKT Photonics, Datasheet, pDF. Accessed: 2026-01-28. [Online]. Available: <https://www.nktphotonics.com/wp-json/nktphotonics/v1/download/Koheras-ADJUSTIK/Koheras%20ADJUSTIK%20and%20ADJUSTIK%20HP%20Datasheet.pdf>